Clays and Clay Minerals, Vol. 69, No. 6:688–701, 2021

INTERFACIAL X-RAY SCATTERING FROM SMALL SURFACES: ADAPTING MINERAL-FLUID STRUCTURE METHODS FOR MICROCRYSTALLINE MATERIALS

Joanne E. Stubbs[1]*, Anna K. Wanhala[1], and Peter J. Eng[1,2]

[1]Center for Advanced Radiation Sources, The University of Chicago, Chicago, IL, USA
[2]James Franck Institute, The University of Chicago, Chicago, IL, USA

Abstract—Crystal truncation rod (CTR) X-ray diffraction is an invaluable tool for measuring mineral surface and adsorbate structures, and has been applied to several environmentally and geochemically important systems. Traditionally, the method has been restricted to single crystals with lateral dimensions >3 mm. Minerals that meet this size criterion represent a minute fraction of those that are relevant to interfacial geochemistry questions, however. Crystal screening, data collection, and CTR measurement methods have been developed for crystals of <0.3 mm in lateral size using the manganese oxide mineral chalcophanite ($ZnMn_3O_7 \cdot 3H_2O$) as a case study. This work demonstrates the feasibility of applying the CTR technique to previously inaccessible surfaces, opening up a large suite of candidate substrates for future study.

Keywords—Birnessite · Crystal truncation rods · Mineral-water interface · Surface structure

INTRODUCTION

Crystal truncation rod (CTR) X-ray scattering probes atomic-level structural details of surfaces and interfaces on single-crystal samples (Fig. 1) (Fenter, 2002; Robinson, 1986). It takes advantage of weak lines or 'rods' of scattered X-ray intensity between Bragg peaks, and perpendicular to crystal surfaces, that encode atom positions and occupancies at interfaces. The technique can be used to determine mineral terminations, the structures of interfacial water layers, and the positions of adsorbates. CTR measurements can be conducted in two geometries. Specular measurements (Fig. 1a) are one-dimensional and probe only the laterally averaged surface-normal electron density, but can determine heights of laterally disordered structures such as layered water. Off-specular measurements (Fig. 1b) allow for the refinement of three-dimensional interfacial structures that are registered with respect to the bulk crystal. Surface scattering signals are many orders of magnitude weaker than bulk Bragg peaks, requiring the use of synchrotron light sources. The University of Chicago GSECARS beamlines 13-BM-C and 13-ID-C at the Advanced Photon Source (APS) at Argonne National Laboratory have been optimized for these experiments. The 13-BM-C beamline has a bending magnet source that operates at fixed energy (either 15 or 28.6 keV) and provides larger blocks of beamtime than the 13-ID-C undulator beamline. The greater accessibility to the 13-BM-C beamline makes it an excellent resource for crystal screening and preliminary measurements, while 13-ID-C offers tunable energy and significantly greater X-ray flux.

To date, CTR has been applied to the surfaces of 18 minerals including four silicates, three carbonates, three phosphates, one sulfate, and seven (oxyhydr) oxides at GSECARS beamlines and others (Table 1). These studies used crystals with lateral surface dimensions typically >3 mm. The CTR approach used to measure these systems previously required large, perfect, single-crystal substrates which intercepted the full X-ray beam footprint at small (2–4°) incidence angle (i.e. the angle made by the incident X-ray beam with respect to the surface of the crystal). In a previous study of the hydrated goethite (100) surface (Ghose et al., 2010), a rare 1 mm×1 mm crystal was measured successfully thanks to the unique X-ray optics developed at GSECARS. The mirrors that supply X-rays to the 13-ID-C endstation are capable of focusing the full APS undulator beam to ~30 μm (full width at half maximum; FWHM), corresponding to a beam footprint on the sample surface of 430–840 μm at 2–4°, allowing the beam footprint to remain within the bounds of the goethite surface. Even when the lateral size requirement is reduced to 1 mm, however, much important science is still inaccessible, as it is nearly impossible to find many minerals with single-crystal surfaces this large.

The conventional constraint of preventing the X-ray beam from overfilling the samples is imposed for two reasons: (1) during off-specular CTR measurements the sample must rotate azimuthally. Preventing spill-off during sample rotation keeps the

* E-mail address of corresponding author: stubbs@cars.uchicago.edu
DOI: 10.1007/s42860-021-00155-4

This article is a product of the 2020 CMS Workshop held in conjunction with the 57th Annual Meeting of The Clay Minerals Society, Richland, Washington, USA.

This manuscript was presented at the 57th Annual Meeting of The Clay Minerals Society as part of its 2020 Workshop on "Emerging Methods in Clay Science" held at Pacific Northwest National Laboratories, Richland, Washington, USA

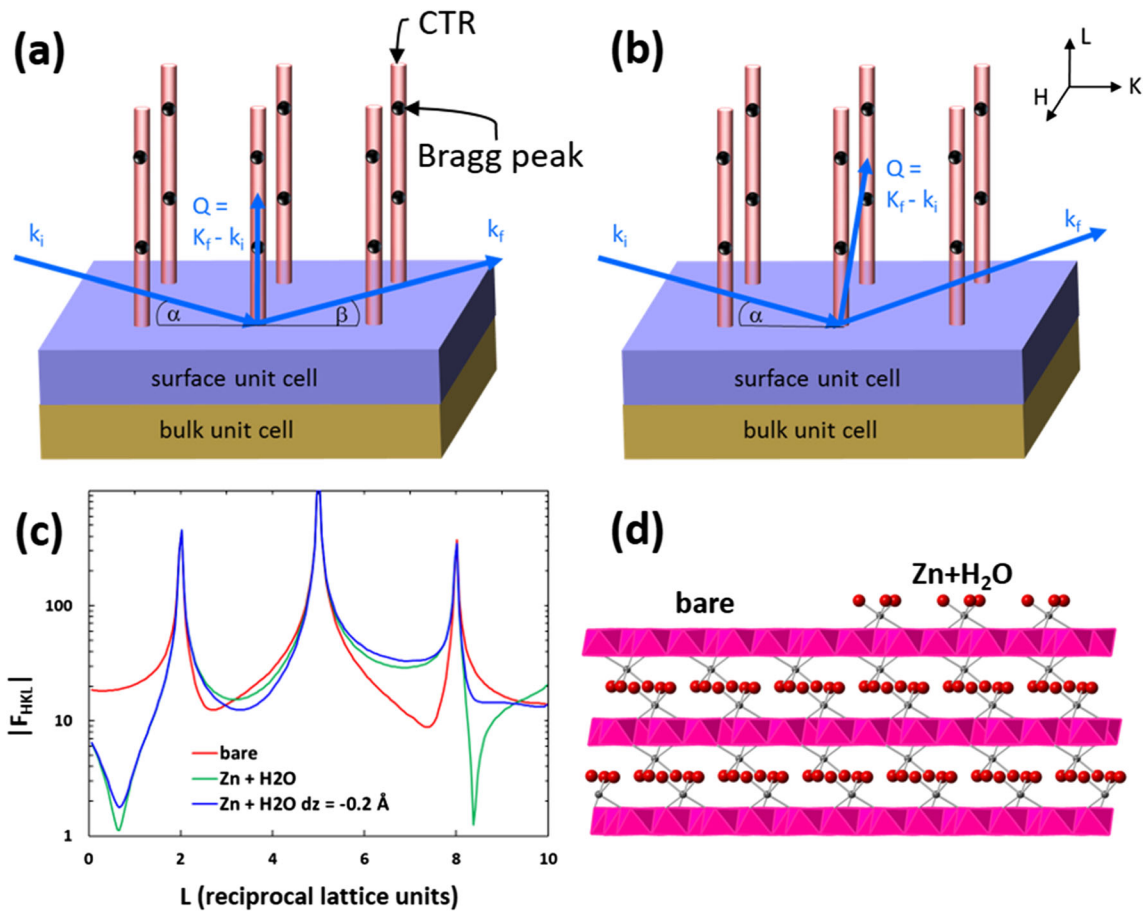

Fig. 1. a, **b**Crystal truncation rods (CTR) are weak lines of X-ray intensity that are perpendicular to the surface and pass through Bragg peaks in reciprocal space. k_i = incident X-ray wave vector; k_f = final scattered wave vector; Q = momentum transfer; α = angle of incidence x-ray beam makes with surface; β = angle of exit; HKL = Miller indices for a surface unit cell with H and K in the surface plane and L normal to it. **a** Specular measurement geometry; α = β, Q ⊥ surface. **b**Off-specular geometry; α fixed, Q has both lateral and surface-normal components. **c** Calculated 20L CTR for chalcophanite ($ZnMn_3O_7{\cdot}3H_2O$) basal plane assuming 'bare' surface (red), surface with Zn and water in bulk positions (green), and surface with Zn and water, as depicted in **d** shifted 0.2 Å toward bulk (blue). CTR profiles are highly sensitive to crystal termination and adsorbate structures

number of surface atoms participating in the scattering constant. (2) Photons that spill off the sample edges will be scattered by the sample holder or other materials. When the number of photons intercepted by the sample surface is comparable to those traversing beyond the sample's edges, the surface diffraction signal becomes difficult to distinguish from the background scattering produced by the sample-support structure.

The present study reports on the development of techniques to measure CTRs from crystals with surfaces a few hundred microns in lateral extent, of sample environments enabling such measurements in the presence of liquids, and of methods for screening microcrystals to identify those of sufficient quality for successful CTR experiments.

METHODS DEVELOPMENT

Methods for Measuring Microcrystals

A method has been pioneered for making CTR measurements from the surfaces of crystals with lateral dimensions as small as 100 μm – an order of magnitude smaller than most previous studies. This is achieved by using the beamline's X-ray optics to adjust the beam footprint so that the entire sample surface is illuminated (thus keeping the number of participating surface atoms fixed). The amount of the beam which 'spills' off the surface is limited to the size needed to illuminate the full sample given eccentricity of the rotation stage, thus minimizing the background scatter from the sample mount. During pilot experiments, background scatter was minimized by attaching samples via electrostatic attraction to high-symmetry, single-crystal substrates composed of low atomic number elements, e.g. diamond or quartz (Fig. 2). The X-ray beam is allowed to spill off of the edges of the microcrystal onto the support crystal, which generates far lower background than typical amorphous or polycrystalline sample cell materials. During specular measurements, the incidence angle varies, and therefore so does the fraction of the beam that spills. Application of a geometric spill-off correction, as is frequently performed for low-angle reflectivity measurements, is relatively straightforward as the crystal does not rotate azimuthally in this measurement mode. The use of single crystals as low-background holders is well established

https://doi.org/10.1007/s42860-021-00155-4 Published online by Cambridge University Press

Table 1. Minerals investigated to date using CTR

Mineral class	Mineral name	Chemical formula	References
Silicates	Quartz	SiO_2	Bellucci et al. (2015),
			Schlegel et al. (2002)
			Park et al. (2005)
	Orthoclase	$KAlSi_3O_8$	Fenter et al. (2000a, 2003a, 2003b, 2008, 2010a, b, Fenter et al., 2014),
			Teng et al. (2001)
	Forsterite	Mg_2SiO_4	Yan et al. (2014)
	Muscovite	$KAl_3Si_3O_{10}(OH)_2$	Bourg et al. (2017)
			Brugman et al. (2018, 2020)
			Cheng et al. (2001)
			de Poel et al. (2014a, 2014b, 2017)
			Fenter et al. (2010a, b)
			Hellebrandt et al. (2016)
			Lee et al. (2007, 2008, 2009, 2010a, 2010b, 2011, 2012, 2013a, 2013b, 2016, 2017, 2019)
			Pintea et al. (2016, 2018)
			Qiu et al. (2018a)
			Schlegel et al. (2006)
			Schmidt et al. (2012a, 2012b, 2013, 2015)
			Stubbs et al. (2019)
			Yuan et al. (2019a)
Carbonates	Calcite	$CaCO_3$	Callagon et al. (2014, 2017)
			Chiarello and Sturchio (1995)
			Fenter and Sturchio (1999, 2012)
			Fenter et al. (2000b, 2013)
			Geissbuhler (2004)
			Heberling et al. (2011, 2014)
			Hofmann et al. (2016)
			Lee et al. (2016)
			Magdans et al. (2006)
	Dolomite	$CaMg(CO_3)_2$	Callagon et al. (2017)
			Fenter et al. (2007)
			La Plante et al. (2018, 2019)
	Rhodochrosite	$MnCO_3$	Jun et al. (2007)
Phosphates	Apatite	$Ca_5(PO_4)_3(OH,F,Cl)$	Pareek et al. (2009)
			Park et al. (2004)
	Archerite	KH_2PO_4	de Vries et al. (1998, 1999)
			Kaminski et al. (2005, 2006)
			Reedijk et al. (2003)
	Xenotime	YPO_4	Stack et al. (2018)
Sulfates	Baryte	$BaSO_4$	Bracco et al. (2017, 2019)
			Fenter et al. (2001)
Oxides	Corundum	Al_2O_3	Catalano (2010, 2011)
			Catalano et al. (2005, 2006a, 2008)
			Eng et al. (2000)

https://doi.org/10.1007/s42860-021-00155-4 Published online by Cambridge University Press

Table 1. (continued)

Mineral class	Mineral name	Chemical formula	References
			Trainor et al. (2002)
			Xu et al. (2018, 2019)
	Hematite	Fe_2O_3	Catalano (2011)
			Catalano et al. (2008)
			Catalano et al. (2006b, 2007a, 2007b, 2009, 2010)
			Lutzenkirchen et al. (2015)
			McBriarty et al. (2017, 2018, 2019)
			Noerpel et al. (2016)
			Qiu et al. (2018b)
			Tanwar et al. (2007a, 2007b, 2008, 2009)
			Trainor et al. (2004)
			Waychunas et al. (2005)
	Magnetite	Fe_3O_4	Petitto et al. (2010)
	Periclase	MgO	Kim and Baik (1994)
			Kim et al. (1993)
			Robach et al. (1998)
	Rutile	TiO_2	Kohli et al. (2010)
			Zhang et al. (2004, 2006, 2007)
	Uraninite	UO_2	Stubbs et al. (2015, 2017)
Oxyhydroxides	Goethite	FeO(OH)	Ghose et al. (2010)

in powder diffraction but has not, to the authors' knowledge, been extended to CTR. This method of mounting and measuring small crystals enabled CTR measurements of the basal plane of the Mn-oxide, chalcophanite ($ZnMn_3O_7{\cdot}3H_2O$). This sheet-structured mineral (Fig. 1d) is a single-crystal proxy for phyllomanganates of the birnessite group, which are important in both energy storage and environmental applications, and are known to sequester significant quantities of contaminant metals from mining and smelting operations (Post & Appleman, 1988; Morin et al., 1999; Post, 1999; Manceau et al., 2000; Hochella et al., 2005; Shope et al., 2006; Vanek et al., 2008; Bargar et al., 2009; Fuller & Bargar, 2014; Post & Heaney, 2014; Kimball et al., 2016).

Chalcophanite crystals from Sterling Hill, New Jersey, were provided by the National Museum of Natural History (Sample C1814). The first crystals were selected on the basis of size, morphology, and visible light surface reflectivity as viewed with an optical microscope. Once selected, crystals were attached by electrostatic attraction to a thin needle or wire. A droplet of deionized water was deposited on the diamond or quartz substrate that had been pre-mounted with beeswax to a 3 mm brass pin (Fig. 2a), then the chalcophanite crystal was deposited in that droplet. Excess water was wicked away with a cotton-tipped swab. The sample assemblies were next inserted into a holder covered with a Kapton dome through which humid helium gas was allowed to flow during measurements (Fig. 2c). Initial experiments revealed angular instability of the mount that diminished over the course of many minutes to an hour, probably resulting from the slow evaporation of thin water layers trapped between the chalcophanite and substrate. Subsequent samples were allowed to dry for >30 min in a laminar flow hood prior to measurement, eliminating this instability.

CTR data sets collected from several crystals showed excellent agreement (Fig. S1, Supplementary Material), demonstrating the viability of the measurements, and indicating that the chalcophanite growth face has a well-defined, consistent surface structure. These initial, proof-of-concept measurements produced exciting results but were somewhat inefficient, due to the labor-intensive process of evaluating the chalcophanite crystals optically, manipulating them onto diamonds, and screening them one-by-one at the beamline. Crystals that have both bulk and surface qualities that are appropriate for CTR are relatively rare and difficult to identify optically but, once mounted, crystals can be evaluated quickly using fast alignment scans of bulk Bragg peaks and brief snapshots of surface X-ray scattering intensities. Thus, the rate-limiting step is the one-by-one mounting procedure itself.

Screening Procedure

A more efficient method has been developed for semi-automatic screening at the 13-BM-C station (Fig. 3). Numerous crystals are deposited on a 30 mm×30 mm quartz wafer (Fig. 3b). The wafer is mounted on a long travel (25 mm) *x*-*y* sample stage with the wafer surface coincident with the diffractometer's center of rotation (Fig. 3a). Positions of

https://doi.org/10.1007/s42860-021-00155-4 Published online by Cambridge University Press

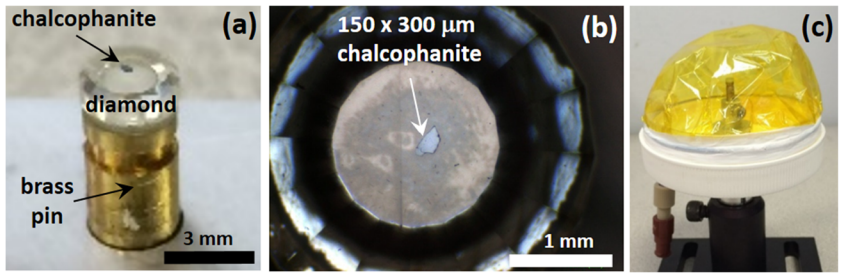

Fig. 2. a Chalcophanite mounted by electrostatic attraction to diamond, which is affixed to a brass pin. **b** Sample crystals <300 µm are mounted readily by this method. **c** Sample is covered by Kapton dome through which humidified helium is allowed to flow during measurement

individual crystals are then mapped using an optical microscope that is centered and focused on the rotation center. The in-plane positions (x, y) are determined using the microscope crosshair (Fig. 3c), and the surface-normal height (z) is determined initially using the depth of focus of the microscope and subsequently refined with X-rays. The sample stage setting (x, y, z) is saved for each crystal. A specular Bragg peak is used for initial alignment. The bulk crystal quality is assessed by measuring the rocking curve of the Bragg peak. In this measurement the crystal is rocked through an angle to determine the width of the diffraction feature with the detector position held fixed. Those with rocking curve FWHM < 0.3° have their alignments refined and CTR intensities are spot-checked at a few points along the specular rod. Crystals are ranked on the basis of bulk and spot-checked surface quality, and those that pass the initial tests undergo three-dimensional alignment and additional CTR measurements. Further observations about crystal and surface quality are recorded, and short CTR data sets, including specular and off-specular data, are collected from the best crystals. These data inform a second ranking scheme that is used to identify candidates for further measurement and experimentation. A typical user experiment at 13-BM-C lasts 3 days, during which >100 crystals may be screened. Roughly 10% of chalcophanite crystals examined in this manner are suitable for further study.

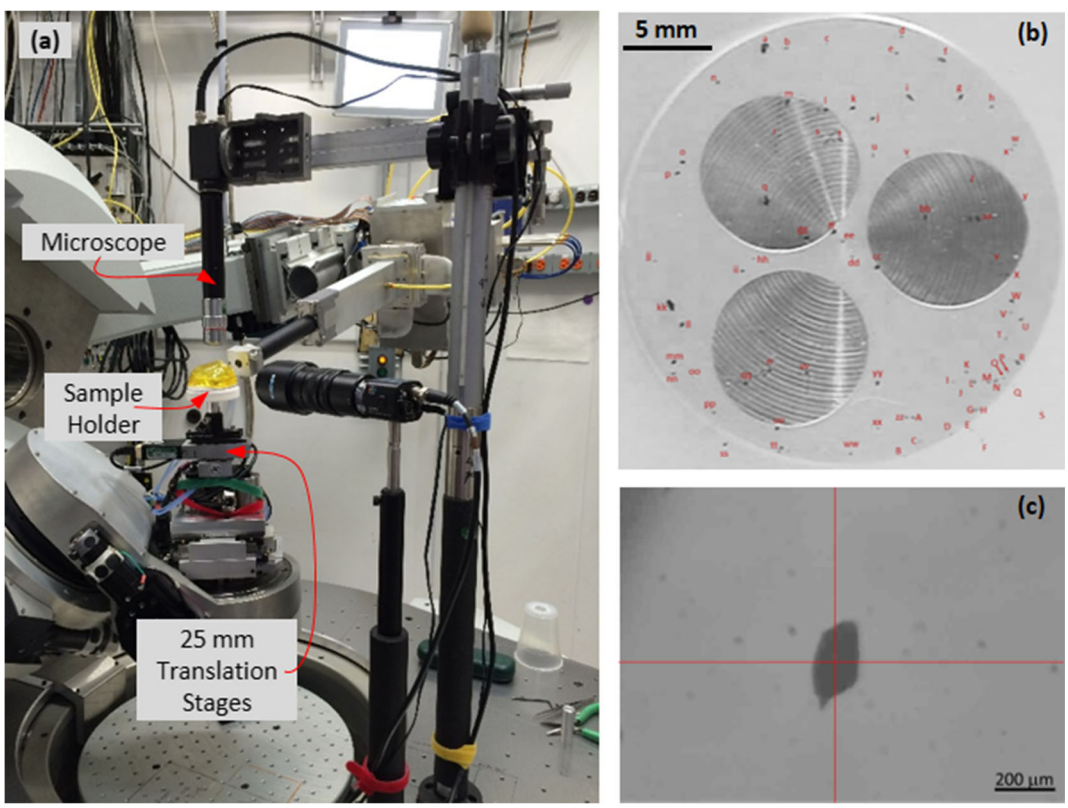

Fig. 3. Crystal screening setup on the diffractometer at beamline 13-BM-C. **a** Samples in Kapton-covered holder are mounted on 25 mm translation stages and viewed with microscope. **b** Chalcophanite crystals are distributed on quartz wafer for efficient screening. **c** Microscope crosshair is used to center crystals on diffractometer rotation axis

https://doi.org/10.1007/s42860-021-00155-4 Published online by Cambridge University Press

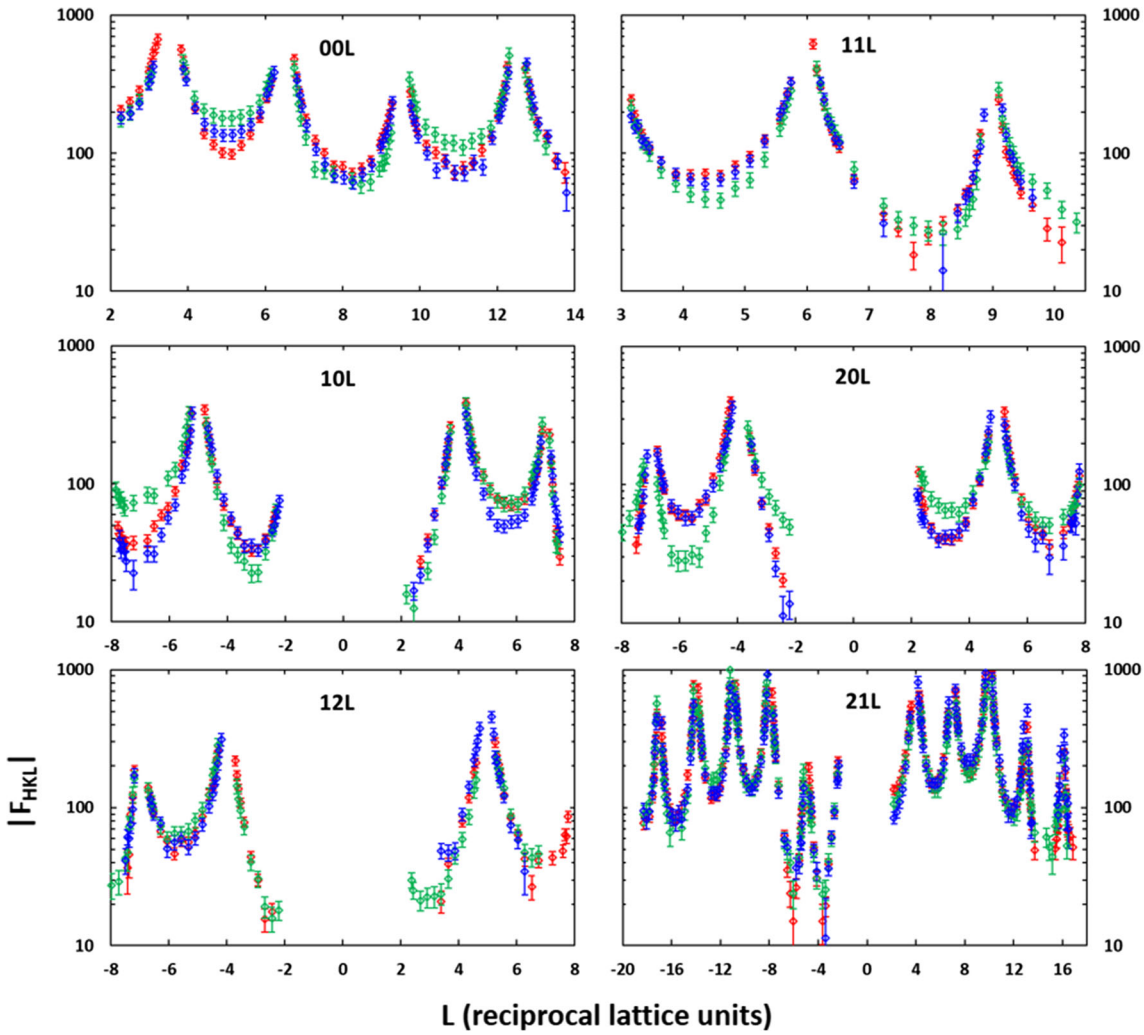

Fig. 4. CTR data collected from a chalcophanite surface in a clean state (red), after dosing with 100 mM CsCl solution (green), and after rinsing with DI water (blue). The 10L, 20L, and 11L rods experienced reversible modifications. Modifications to the 00L (specular) rod were partially reversed upon rinsing.

Ex situ Adsorption

In addition to measurement of the untreated growth surface, the feasibility of adsorption experiments was also tested. Crystals were exposed to a 100 mM solution of CsCl (Alfa Aesar, Haverhill, Massachusetts, USA), wicked dry, and measured in the same humid He environment as the untreated growth surfaces. Modifications were observed on both specular and off-specular rods (Fig. 4) that were reproducible across multiple crystals. For changes to appear on the off-specular rods, adsorption must occur in a manner that is laterally registered with respect to the bulk. Upon rinsing with DI water, the off-specular CTRs returned to their original, untreated profiles (Fig. 4), while the specular CTR recovered partially. These results indicated that the laterally registered Cs sorption was reversible. They also suggested that the Cs atoms did not replace surface Zn atoms. Had they done so, the off-specular CTRs would not have returned to their original profiles after rinsing. Additional crystals were exposed to solutions of $ZnCl_2$ and $Zn(NO_3)_2$ (Alfa Aesar, Haverhill, Massachusetts, USA), again resulting in modifications to both specular and off-specular CTRs (Fig. S2), including regions of reciprocal space other than those affected by CsCl. This suggests structurally different adsorbate conformations for the Cs^+ and Zn^{2+}. In the case of the Zn-bearing solutions, powder diffraction rings were observed indicating the precipitation of powders on the mineral surface and highlighting the need for environmental cells that retain liquid solution in contact with microcrystal surfaces for in situ measurements.

Mounting Crystals for in situ Measurements

Static adhesion to diamond and quartz substrates is an excellent method for mounting microcrystals for measurement in a gas-filled environment, but cannot be used when exposure to aqueous solutions is required, as is the case for many geochemical investigations. While large crystals can be held in place by the same thin Kapton membranes that are used to

https://doi.org/10.1007/s42860-021-00155-4 Published online by Cambridge University Press

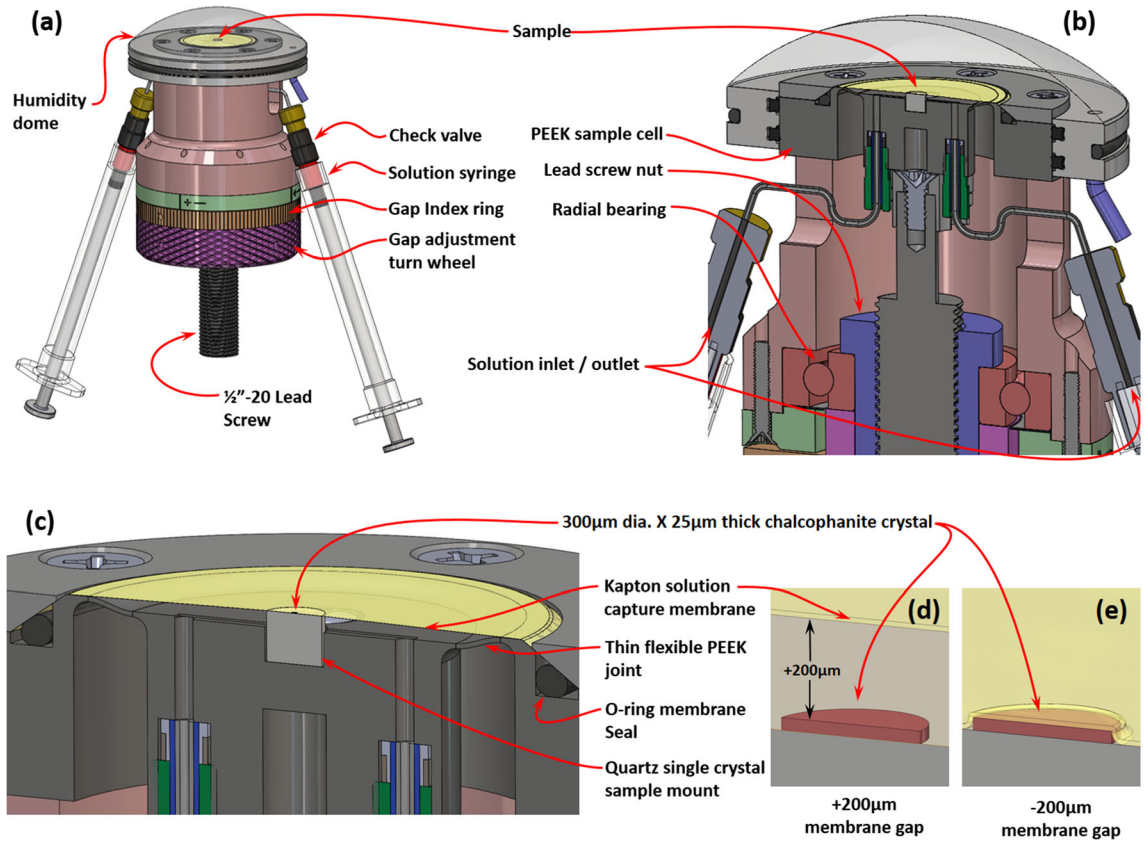

Fig. 5. Liquid cell. **a** Full cell with solution connections, humidity dome, lead screw, and gap-adjustment turn wheel. **b** PEEK sample cell, lead screw nut, and radial bearing. **c** Quartz single crystal sample mount, microcrystal sample, thin flexible PEEK joint, and Kapton solution capture membrane. **d** Sample cell set to a positive membrane gap so that reactions can occur under a thick layer of bulk solution. **e** Sample cell set to a negative gap that traps a solution layer a few microns thick and lowers the rim of the cell below the sample surface to allow X-ray access at low incident and scattering angles

hold liquids on their surfaces (Fenter, 2002; Stubbs et al., 2019), this strategy falls short for microcrystals, especially when the back surface of the crystal is rough or stepped. Early attempts using this method revealed that pulling a membrane tightly against chalcophanite microcrystals results in significant strain or fracture, and indicated the need for a robust, but more gentle means of affixing a crystal that is independent of the film that holds the liquid in place. This motivated a search for an adhesive that can be used to mount these inherently difficult to handle microcrystals. Thermoplastic resins such as Crystalbond™ are used frequently in CTR measurements of larger crystals, but their use is not feasible when the crystal

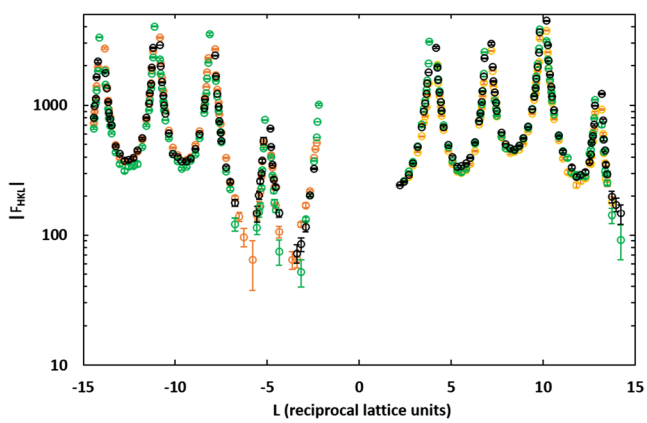

Fig. 6. 21L and symmetry equivalent CTRs show excellent agreement. Data are from a crystal mounted on a quartz substrate using UV-cured adhesive and measured under water in the new, in situ cell

https://doi.org/10.1007/s42860-021-00155-4 Published online by Cambridge University Press

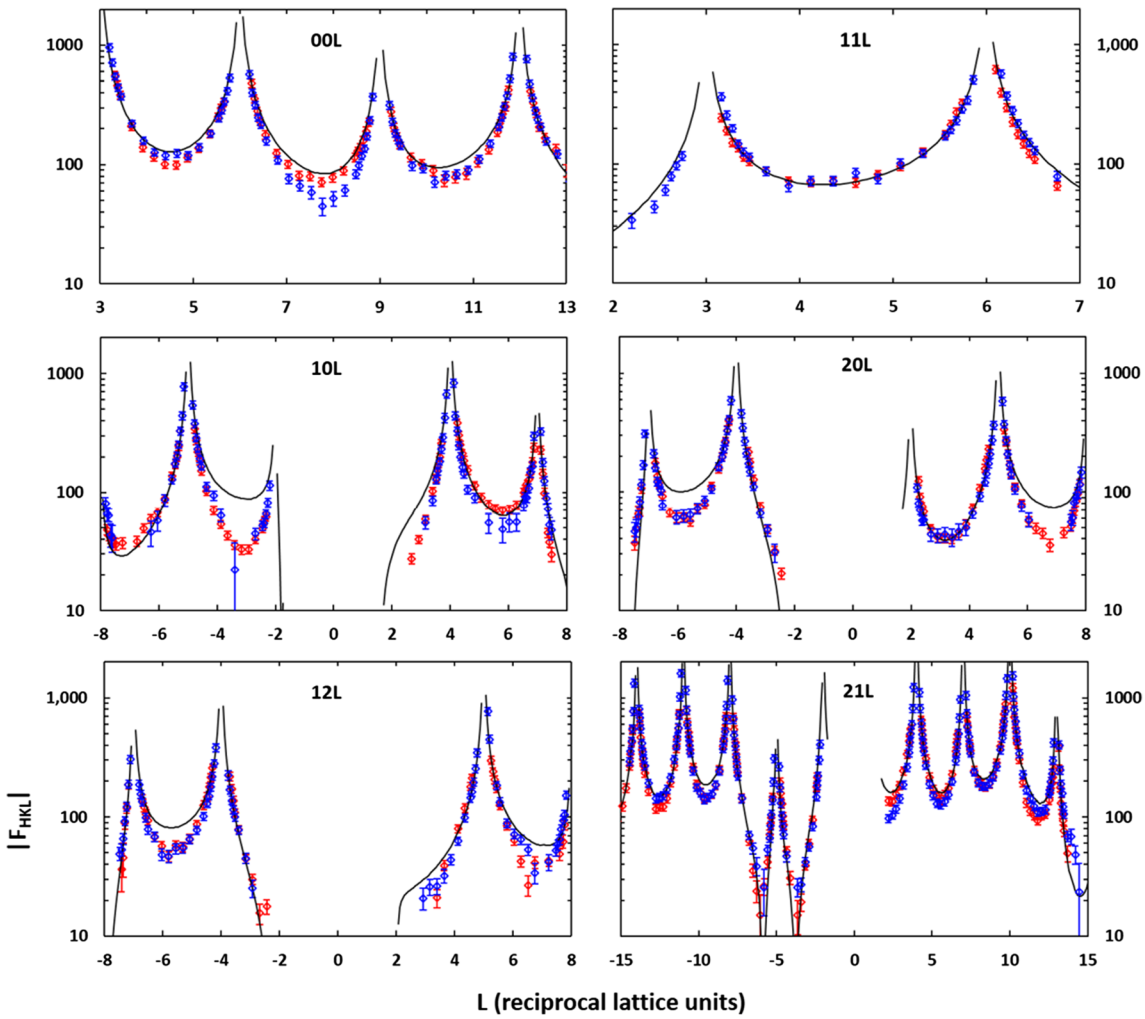

Fig. 7. Data collected from a chalcophanite crystal affixed to quartz with UV adhesive under deionized water (blue) are qualitatively similar to those collected from a different crystal attached by static attraction to diamond under humid helium (red). Black curves are calculated CTRs from a model that includes a layer of Zn and water at the surface, as shown in Fig. 1d, with no roughness or relaxation of atoms from bulk positions and occupancies

must be manipulated with a needle and positioned under a microscope.

A process has been optimized for depositing 100–300 μm crystals onto similarly sized droplets of UV-cured adhesive, and curing with UV light from behind**.** Several UV adhesives from multiple vendors were evaluated, and the most successful was Norland Optical Adhesives (Cranbury, New Jersey, USA) NOA86. A UV cure box (FormCure, Formlabs, Somerville, Massachusetts, USA) has been modified to replace the standard 405 nm wavelength LEDs with 365 nm wavelength LEDs, and the adhesive is cured overnight at a temperature of 60°C. It is then allowed to sit in fluorescent room light for several days while polymerization continues. Chalcophanite CTRs measured after UV curing by this method are very similar to those measured before, indicating that the crystal is undamaged and the ordered part of the surface is unchanged. Other minerals, however, could possibly experience damage and the method should be validated when applied to new systems.

Quartz single crystals are highly transparent to 365 nm UV light, aiding with adhesive curing, and are chemically inert, making them excellent substrates for aqueous surface chemistry experiments. Quartz wafers oriented to the (5-1-1) surface are commercially available as 'no background' holders for powder diffraction experiments (MTI Corp., Richmond, California, USA). In this orientation, the first Bragg reflection in the specular direction is at L ~22.7 for chalcophanite, mitigating interferences between quartz Bragg peaks and the chalcophanite specular CTR. Sometimes interferences are observed between low-angle quartz reflectivity and the lowest-L region of the specular CTR. This is usually alleviated by a mismount or tilt of the microcrystal (due to steps or

https://doi.org/10.1007/s42860-021-00155-4 Published online by Cambridge University Press

protuberances on the back side) with respect to the quartz surface of several tenths of a degree, which makes separation of the two signals straightforward, and the quartz reflectivity is simply excluded during data integration. For off-specular CTRs, it would take an extraordinary coincidence in alignment to produce overlap of a Bragg peak or CTR from the quartz with a CTR from the microcrystal, although occasionally thermal diffuse scatter from nearby quartz Bragg peaks interferes over small regions of reciprocal space. These regions are excluded from the data sets. Far from quartz Bragg peaks, diffuse scatter arising from the quartz single crystal is weak and broad when compared to CTRs, and is easily subtracted as background.

In situ Sample Environment

Quartz wafers 2.5 mm thick are core drilled into cylinders with 3 mm diameters, which are clamped rigidly inside a PEEK sample cell (Fig. 5). This cell includes two ports for solution injection and extraction, which are capped with Luer Lock check valve fittings (Idex Health and Science, Oak Harbor, Washington, USA) such that solution exchanges can be made with syringes that are disconnected prior to measurement (Fig. 5a). The central post into which the quartz cylinder is clamped is supported rigidly on a ½ inch - 20 lead screw, which is itself mounted rigidly on the diffractometer. Solution is held in place by a Kapton membrane that is attached to an outer ring which surrounds the inner post (Fig. 5c, d, e). The two sections of the cell (post and membrane support) are machined from a single piece of PEEK, and are connected by a thin, flexible PEEK joint (Fig. 5c). The Kapton membrane is raised and lowered with respect to the sample surface by means of a nut that rides on the central lead screw, flexing the thin PEEK joint. This mechanism is hand-actuated using the gap adjustment turn wheel (Fig. 5a). Prior to solution injection, the membrane is raised to produce a gap between Kapton and sample (Fig. 5d), such that reactions can occur under several hundred microns of bulk solution. Prior to measurement, solution is extracted by closing one check valve and gently withdrawing liquid through the other while lowering the membrane ring to a height below the sample surface (negative gap), trapping a layer of solution a few microns thick (as verified by the appearance of visible-light interference fringes, i.e. Newton's rings) (Fig. 5e). To mitigate diffusion and evaporation of water through the Kapton membrane, humidified helium is flowed through a domed Mylar membrane cover (Fig. 5a). This cell design is conceptually similar to a previous cell (Trainor et al., 2006), but offers a simplified, easy to manufacture and customizable cell that can be modified to match sample size. The manually driven nut mechanism replaces an earlier motorized stage, making it possible to produce multiple cells quickly and inexpensively. The new cell's PEEK flexure joint between the sample support post and membrane eliminates, from the earlier design, a sliding O-ring seal that was often a source of solution leaks and excess sliding friction.

Stability During in situ Measurements

The UV adhesive mounts are dimensionally stable in the X-ray beam under dry and humid gas, and also stable for many hours in liquid water in the absence of X-rays. The microcrystal alignment drifts gradually over time in the presence of both X-rays and water, however, indicating that the adhesive is sensitive to the products of X-ray-induced water radiolysis. A software solution was developed that realigns the crystal using two Bragg peaks on each CTR immediately prior to its measurement, enabling automatic correction for slowly drifting alignments during data collection. Symmetry-equivalent CTRs show excellent agreement (Fig. 6), indicating that the software alignment correction is effective, and the practice of allowing the beam to overfill the sample surface and spill over the edges results in uniform illumination, even during the azimuthal rotation required for off-specular measurements. Data collected from chalcophanite crystals under deionized water are qualitatively similar to those measured under humid helium (Fig. 7), indicating that the beam damage to the adhesive does not result in ordered modification of the surface, although the deposition of disordered contaminants cannot be ruled out. CTRs calculated from a model with Zn and water molecules at the surface, as shown in Fig. 1d (with no roughness or relaxation of atoms from bulk positions) reproduce measured intensities near Bragg peaks and over much of the CTRs between them (Fig. 7). Discrepancies between the model and data result from differences between the real interfacial structure and this simplified, idealized model. Quantitative fitting of an atomic scale model is ongoing and will be the subject of a separate publication. Measurements designed to probe in situ adsorption and cation exchange are also under way, using solutions containing Cs^{+}, Zn^{2+}, and other cations.

DISCUSSION AND OUTLOOK

The ability to measure CTRs from crystals with lateral dimensions as small as 100 μm, especially in the presence of liquid water, expands significantly the range of candidate synthetic and natural mineral surfaces that can be studied, and represents a major advance in the technique. The next stages of development will target even smaller crystals, which pose challenges with respect to sample handling, adhesive deposition, and signal-to-background ratios as the number of surface atoms decreases.

A second set of considerations arises around the thickness of the crystals being measured, and whether the measurement will probe both the front and back surfaces. CTR measurements are usually made at X-ray energies from 10 to 20 keV, and off-specular data are typically collected at an X-ray incidence angle, α, between 2 and 6°. At 15 keV and $\alpha = 4°$, a chalcophanite crystal would need to be >23 μm thick in order to prevent 99% of incident X-rays from reaching the back surface – a criterion more than sufficient to prevent scattering from the back surface from contributing to the measurement.

https://doi.org/10.1007/s42860-021-00155-4 Published online by Cambridge University Press

Because X-ray absorption depends on density and atomic number in addition to incident energy and path length, the importance of these effects varies widely for different materials. At 15 keV and $\alpha = 4°$, uraninite (UO_2) would require a thickness of ~2 μm whereas quartz would require >200 μm to satisfy the 99% absorption criterion. That criterion overestimates the contribution from the back surface, as X-rays that diffract from a back surface with sufficiently low roughness to present a strong CTR would need to travel back through the thickness of the crystal to be measured. Along this path these X-rays would be subject to diffuse scattering by the bulk microcrystal, further diminishing the CTR signal. Furthermore, some of the X-rays that reach the back surface will exit the microcrystal and be absorbed or scattered by the quartz substrate, and thus be unavailable for return to the front. The contribution from the back surface can be evaluated by reducing α, thus increasing the X-ray path length through the crystal, or by lowering X-ray energy and utilizing the inverse energy cubed dependence of absorption. Specular CTR measurements vary the incidence angle over a wide range, and therefore require extra care in their interpretation when thin crystals with high quality back surfaces are involved. Here again, measurements collected at multiple energies would be highly effective for evaluating the strength of such contributions.

Even with the newly expanded capabilities described here, some crystals remain too small for CTR, and other methods must be employed. Promising among these are those that leverage X-ray coherence, such as Bragg Coherent Diffraction Imaging (BCDI) (Robinson et al., 2001; Pfeifer et al., 2006; Williams et al., 2006). This technique has been used to investigate morphology, defects, strain, and structural responses to aqueous chemistry in mineral nanoparticles including calcite (Clark et al., 2015; Ihli et al., 2016, 2019; Liu et al., 2018) and magnetite (Yuan et al., 2019b). Upgrades are planned or underway for a number of synchrotron facilities, including the APS, that will increase X-ray coherence by roughly two orders of magnitude. Such advances will render the coherent techniques both more powerful and more routinely available to synchrotron users, including members of the Earth Science community.

CONCLUSIONS

Capabilities for screening, mounting, and measuring crystal truncation rods from mineral crystals with lateral dimensions of <300 μm have been developed at the University of Chicago GSECARS beamlines located at the Advanced Photon Source. More than 100 crystals at a time can be screened for bulk and surface quality. The best of these are mounted using UV adhesive onto quartz substrates and clamped in novel environmental cells, enabling exposure to aqueous solutions for in-situ mineral-water interfacial structural measurements. These new capabilities promise to expand dramatically the list of minerals accessible to investigation using CTR.

ACKNOWLEDGMENTS

The authors thank Dr. Jeffrey E. Post at the National Museum of Natural History for providing chalcophanite crystals as well as fruitful discussions. Instrumentation developments, measurements, and analysis were supported by U.S. Department of Energy (DOE), Basic Energy Sciences (BES), Chemical Sciences, Geosciences, and Biosciences (CSGB) Division, Geosciences program (DE-FG02-94ER14466 and DE-SC0019108). CTR measurements were made at GeoSoilEnviroCARS, The University of Chicago – a user facility supported by the National Science Foundation, Earth Sciences (EAR – 1634415). GeoSoilEnviroCARS is located at the Advanced Photon Source, a DOE Office of Science User Facility operated by Argonne National Laboratory under Contract No. DE-AC02-06CH11357.

FUNDING

Funding sources are as stated in the Acknowledgments.

Declarations

Conflict of Interest

The authors declare that they have no conflict of interest.

REFERENCES

Bargar, J. R., Fuller, C. C., Marcus, M. A., Brearley, A. J., De la Rosa, M. P., Webb, S. M., & Caldwell, W. A. (2009). Structural characterization of terrestrial microbial Mn oxides from Pinal Creek, AZ. *Geochimica et Cosmochimica Acta, 73*(4), 889–910. https://doi.org/10.1016/j.gca.2008.10.036

Bellucci, F., Lee, S., Kubicki, J., Bandura, A., Zhang, Z., Wesolowski, D., & Fenter, P. (2015). Rb^+ adsorption at the quartz(101)-aqueous interface: Comparison of resonant anomalous x-ray reflectivity with ab initio calculations. *Journal of Physical Chemistry C, 119*(9), 4778–4788. https://doi.org/10.1021/jp510139t

Bourg, I., Lee, S., Fenter, P., & Tournassat, C. (2017). Stern layer structure and energetics at mica-water interfaces. *Journal of Physical Chemistry C, 121*(17), 9402–9412. https://doi.org/10.1021/acs.jpcc.7b01828

Bracco, J. N., Lee, S. S., Stubbs, J. E., Eng, P. J., Heberling, F., Fenter, P., & Stack, A. G. (2017). Hydration structure of the barite (001)-water interface: Comparison of x-ray Reflectivity with molecular dynamics simulations. *Journal of Physical Chemistry C, 121*(22), 12236–12248. https://doi.org/10.1021/acs.jpcc.7b02943

Bracco, J., Lee, S., Stubbs, J., Eng, P., Jindra, S., Warren, D., Kommu, A., Fenter, P., Kubicki, J., & Stack, A. (2019). Simultaneous adsorption and incorporation of Sr^{2+} at the barite (001)-water interface. *Journal of Physical Chemistry C, 123*(2), 1194–1207. https://doi.org/10.1021/acs.jpcc.8b08848

Brugman, S., Townsend, E., Smets, M., Accordini, P., & Vlieg, E. (2018). Concentration-dependent adsorption of CsI at the muscovite-electrolyte interface. *Langmuir, 34*(13), 3821–3826. https://doi.org/10.1021/acs.langmuir.8b00038

Brugman, S. J. T., Werkhoven, B. L., Townsend, E. R., Accordini, P., van Roij, R., & Vlieg, E. (2020). Monovalent-divalent cation competition at the muscovite mica surface: Experiment and theory. *Journal of Colloid and Interface Science, 559*, 291–303. https://doi.org/10.1016/j.jcis.2019.10.009

Callagon, E., Fenter, P., Nagy, K., & Sturchio, N. (2014). Incorporation of Pb at the calcite (104)-water interface. *Environmental Science & Technology, 48*(16), 9263–9269. https://doi.org/10.1021/es5014888

https://doi.org/10.1007/s42860-021-00155-4 Published online by Cambridge University Press

Callagon, E., Lee, S., Eng, P., Laanait, N., Sturchio, N., Nagy, K., & Fenter, P. (2017). Heteroepitaxial growth of cadmium carbonate at dolomite and calcite surfaces: Mechanisms and rates. *Geochimica et Cosmochimica Acta, 205*, 360–380. https://doi.org/10.1016/j.gca.2016.12.007

Catalano, J. (2010). Relaxations and interfacial water ordering at the corundum (110) Surface. *Journal of Physical Chemistry C, 114*(14), 6624–6630. https://doi.org/10.1021/jp100455s

Catalano, J. (2011). Weak interfacial water ordering on isostructural hematite and corundum (001) surfaces. *Geochimica et Cosmochimica Acta, 75*(8), 2062–2071. https://doi.org/10.1016/j.gca.2011.01.025

Catalano, J., Trainor, T., Eng, P., Waychunas, G., & Brown, G. (2005). CTR diffraction and grazing-incidence EXAFS study of U(VI) adsorption onto alpha-Al_2O_3 and alpha-Fe_2O_3 (1(1)over-bar02) surfaces. *Geochimica et Cosmochimica Acta, 69*(14), 3555–3572. https://doi.org/10.1016/j.gca.2005.03.044

Catalano, J., Park, C., Zhang, Z., & Fenter, P. (2006a). Termination and water adsorption at the alpha-Al_2O_3(012) - Aqueous solution interface. *Langmuir, 22*(10), 4668–4673. https://doi.org/10.1021/la060177s

Catalano, J., Zhang, Z., Fenter, P., & Bedzyk, M. (2006b). Inner-sphere adsorption geometry of Se(IV) at the hematite (100)-water interface. *Journal of Colloid and Interface Science, 297*(2), 665–671. https://doi.org/10.1016/j.jcis.2005.11.026

Catalano, J., Zhang, Z., Park, C., Fenter, P., & Bedzyk, M. (2007a). Bridging arsenate surface complexes on the hematite (012) surface. *Geochimica et Cosmochimica Acta, 71*(8), 1883–1897. https://doi.org/10.1016/j.gca.2007.01.015

Catalano, J., Fenter, P., & Park, C. (2007b). Interfacial water structure on the (012) surface of hematite: Ordering and reactivity in comparison with corundum. *Geochimica et Cosmochimica Acta, 71*(22), 5313–5324. https://doi.org/10.1016/j.gca.2007.09.019

Catalano, J., Park, C., Fenter, P., & Zhang, Z. (2008). Simultaneous inner- and outer-sphere arsenate adsorption on corundum and hematite. *Geochimica et Cosmochimica Acta, 72*(8), 1986–2004. https://doi.org/10.1016/j.gca.2008.02.013

Catalano, J., Fenter, P., & Park, C. (2009). Water ordering and surface relaxations at the hematite (110)-water interface. *Geochimica et Cosmochimica Acta, 73*(8), 2242–2251. https://doi.org/10.1016/j.gca.2009.02.001

Catalano, J., Fenter, P., Park, C., Zhang, Z., & Rosso, K. (2010). Structure and oxidation state of hematite surfaces reacted with aqueous Fe(II) at acidic and neutral pH. *Geochimica et Cosmochimica Acta, 74*(5), 1498–1512. https://doi.org/10.1016/j.gca.2009.12.018

Cheng, L., Fenter, P., Nagy, K., Schlegel, M., & Sturchio, N. (2001). Molecular-scale density oscillations in water adjacent to a mica surface. *Physical Review Letters, 87*(15), Article ARTN 156103. https://doi.org/10.1103/PhysRevLett.87.156103

Chiarello, R. P., & Sturchio, N. C. (1995). The calcite (10-14) cleavage surface in water - early results of a crystal truncation rod study. *Geochimica et Cosmochimica Acta, 59*(21), 4557–4561. https://doi.org/10.1016/0016-7037(95)00363-5

Clark, J. N., Ihli, J., Schenk, A. S., Kim, Y. Y., Kulak, A. N., Campbell, J. M., Nisbet, G., Meldrum, F., & Robinson, I. K. (2015). Three-dimensional imaging of dislocation propagation during crystal growth and dissolution. *Nature Materials*, *14*(8), 780-+. https://doi.org/10.1038/nmat4320

de Poel, W., Pintea, S., de Jong, A., Drnec, J., Carla, F., Felici, R., & 5 others. (2014a). Dibenzo crown ether layer formation on muscovite mica. *Langmuir, 30*(42), 12570–12577. https://doi.org/10.1021/la502879z

de Poel, W., Pintea, S., Drnec, J., Carla, F., Felici, R., Mulder, P., & 4 others. (2014b). Muscovite mica: Flatter than a pancake. *Surface Science, 619*, 19–24. https://doi.org/10.1016/j.susc.2013.10.008

de Poel, W., Vaessen, S., Drnec, J., Engwerda, A., Townsend, E., Pintea, S., & 8 others. (2017). Metal ion-exchange on the muscovite mica surface. *Surface Science, 665*, 56–61. https://doi.org/10.1016/j.susc.2017.08.013

de Vries, S. A., Goedtkindt, P., Bennett, S. L., Huisman, W. J., Zwanenburg, M. J., Smilgies, D. M., et al. (1998). Surface atomic structure of KDP crystals in aqueous solution: An explanation of the growth shape. *Physical Review Letters, 80*(10), 2229–2232. https://doi.org/10.1103/PhysRevLett.80.2229

de Vries, S. A., Goedtkindt, P., Huisman, W. J., Zwanenburg, M. J., Feidenhans'l, R., Bennett, S. L., ... Vlieg, E. (1999). X-ray diffraction studies of potassium dihydrogen phosphate (KDP) crystal surfaces. *Journal of Crystal Growth*, *205*(1–2), 202–214. https://doi.org/10.1016/s0022-0248(99)00249-3

Eng, P., Trainor, T., Brown, G., Waychunas, G., Newville, M., Sutton, S., & Rivers, M. (2000). Structure of the hydrated alpha-Al_2O_3(0001) surface. *Science, 288*(5468), 1029–1033. https://doi.org/10.1126/science.288.5468.1029

Fenter, P. (2002). X-ray reflectivity as a probe of mineral-fluid interfaces: A user guide [Article|Proceedings Paper]\. *Applications of Synchrotron Radiation in Low-Temperature Geochemistry and Environmental Sciences, 49*, 149–220. https://doi.org/10.2138/gsrmg.49.1.149

Fenter, P., & Sturchio, N. (1999). Structure and growth of stearate monolayers on calcite: First results of an in situ X-ray reflectivity study. *Geochimica et Cosmochimica Acta, 63*(19–20), 3145–3152. https://doi.org/10.1016/S0016-7037(99)00241-0

Fenter, P., & Sturchio, N. (2012). Calcite (104)-water interface structure, revisited. *Geochimica et Cosmochimica Acta, 97*, 58–69. https://doi.org/10.1016/j.gca.2012.08.021

Fenter, P., Teng, H., Geissbuhler, P., Hanchar, J., Nagy, K., & Sturchio, N. (2000a). Atomic-scale structure of the orthoclase (001)-water interface measured with high-resolution X-ray reflectivity. *Geochimica et Cosmochimica Acta, 64*(21), 3663–3673. https://doi.org/10.1016/S0016-7037(00)00455-5

Fenter, P., Geissbuhler, P., DiMasi, E., Srajer, G., Sorensen, L., & Sturchio, N. (2000b). Surface speciation of calcite observed in situ by high-resolution X-ray reflectivity. *Geochimica et Cosmochimica Acta, 64*(7), 1221–1228. https://doi.org/10.1016/S0016-7037(99)00403-2

Fenter, P., McBride, M., Srajer, G., Sturchio, N., & Bosbach, D. (2001). Structure of barite (001)- and (210)-water interfaces. *Journal of Physical Chemistry B, 105*(34), 8112–8119. https://doi.org/10.1021/jp0105600

Fenter, P., Cheng, L., Park, C., Zhang, Z., & Sturchio, N. (2003a). Structure of the orthoclase (001)- and (010)-water interfaces by high-resolution X-ray reflectivity. *Geochimica et Cosmochimica Acta, 67*(22), 4267–4275. https://doi.org/10.1016/S0016-7037(03)00374-0

Fenter, P., Park, C., Cheng, L., Zhang, Z., Krekeler, M., & Sturchio, N. (2003b). Orthoclase dissolution kinetics probed by in situ X-ray reflectivity: Effects of temperature, pH, and crystal orientation. *Geochimica et Cosmochimica Acta, 67*(2), 197–211, Article PII S0016-7037(02)01084-0. https://doi.org/10.1016/S0016-7037(02)01084-0

Fenter, P., Zhang, Z., Park, C., Sturchio, N., Hu, X., & Higgins, S. (2007). Structure and reactivity of the dolomite (104)-water interface: New insights into the dolomite problem. *Geochimica et Cosmochimica Acta, 71*(3), 566–579. https://doi.org/10.1016/j.gca.2006.10.006

Fenter, P., Park, C., & Sturchio, N. (2008). Adsorption of Rb^+ and Sr^{2+} at the orthoclase (001)-solution interface. *Geochimica et Cosmochimica Acta, 72*(7), 1848–1863. https://doi.org/10.1016/j.gca.2007.12.016|10.1016/j.uca.2007.12.016

Fenter, P., Lee, S., Park, C., Catalano, J., Zhang, Z., & Sturchio, N. (2010a). Probing interfacial reactions with X-ray reflectivity and X-ray reflection interface microscopy: Influence of NaCl on the dissolution of orthoclase at pOH 2 and 85 degrees C. *Geochimica et Cosmochimica Acta, 74*(12), 3396–3411. https://doi.org/10.1016/j.gca.2010.03.027

Fenter, P., Lee, S., Park, C., Soderholm, L., Wilson, R., & Schwindt, O. (2010b). Interaction of muscovite (001) with Pu3+ bearing solutions at pH 3 through ex-situ observations. *Geochimica et Cosmochimica*

Acta, 74(24), 6984–6995. https://doi.org/10.1016/j.gca.2010.09.025

Fenter, P., Kerisit, S., Raiteri, P., & Gale, J. (2013). Is the Calcite-Water Interface Understood? Direct comparisons of molecular dynamics simulations with specular x-ray reflectivity data. *Journal of Physical Chemistry C, 117*(10), 5028–5042. https://doi.org/10.1021/jp310943s

Fenter, P., Zapol, P., He, H., & Sturchio, N. (2014). On the variation of dissolution rates at the orthoclase (001) surface with pH and temperature. *Geochimica et Cosmochimica Acta, 141*, 598–611. https://doi.org/10.1016/j.gca.2014.06.019

Fuller, C. C., & Bargar, J. R. (2014). Processes of zinc attenuation by biogenic manganese oxides forming in the hyporheic zone of Pinal Creek, Arizona. *Environmental Science & Technology, 48*(4), 2165–2172. https://doi.org/10.1021/es402576f

Geissbuhler, P., Fenter, P., DiMasi, E., Srajer, G., Sorensen, L., & Sturchio, N. (2004). Three-dimensional structure of the calcite-water interface by surface X-ray scattering. *Surface Science, 573*(2), 191–203. https://doi.org/10.1016/j.susc.2004.09.036

Ghose, S. K., Waychunas, G. A., Trainor, T. P., & Eng, P. J. (2010). Hydrated goethite (alpha-FeOOH) (100) interface structure: Ordered water and surface functional groups. *Geochimica et Cosmochimica Acta, 74*(7), 1943–1953. https://doi.org/10.1016/j.gca.2009.12.015

Heberling, F., Trainor, T., Lutzenkirchen, J., Eng, P., Denecke, M., & Bosbach, D. (2011). Structure and reactivity of the calcite-water interface. *Journal of Colloid and Interface Science, 354*(2), 843–857. https://doi.org/10.1016/j.jcis.2010.10.047

Heberling, F., Eng, P., Denecke, M., Lutzenkirchen, J., & Geckeis, H. (2014). Electrolyte layering at the calcite(104)-water interface indicated by Rb^{+}- and Se(VI) K-edge resonant interface diffraction. *Physical Chemistry Chemical Physics, 16*(25), 12782–12792. https://doi.org/10.1039/c4cp00672k

Hellebrandt, S., Lee, S. S., Knope, K. E., Lussier, A. J., Stubbs, J. E., Eng, P. J., Soderholm, L., Fenter, P., & Schmidt, M. (2016). A comparison of adsorption, reduction, and polymerization of the plutonyl(VI) and uranyl(VI) Ions from solution onto the muscovite basal plane. *Langmuir, 32*(41), 10473–10482. https://doi.org/10.1021/acs.langmuir.6b02513

Hochella, M. F., Kasama, T., Putnis, A., Putnis, C. V., & Moore, J. N. (2005). Environmentally important, poorly crystalline Fe/Mn hydrous oxides: Ferrihydrite and a possibly new vernadite-like mineral from the Clark Fork River Superfund Complex. *American Mineralogist, 90*(4), 718–724. https://doi.org/10.2138/am.2005.1591

Hofmann, S., Voitchovsky, K., Spijker, P., Schmidt, M., & Stumpf, T. (2016). Visualising the molecular alteration of the calcite (104) – water interface by sodium nitrate. *Scientific Reports, 6*, Article 21576. https://doi.org/10.1038/srep21576

Ihli, J., Clark, J. N., Cote, A. S., Kim, Y. Y., Schenk, A. S., Kulak, A. N., & 6 others. (2016). Strain-relief by single dislocation loops in calcite crystals grown on self-assembled monolayers. *Nature Communications, 7*, Article 11878. https://doi.org/10.1038/ncomms11878

Ihli, J., Clark, J. N., Kanwal, N., Kim, Y. Y., Holden, M. A., Harder, R. J., Tang, C. C., Ashbrook, S. E., Robinson, I. K., & Meldrum, F. C. (2019). Visualization of the effect of additives on the nanostructures of individual bio-inspired calcite crystals. *Chemical Science, 10*(4), 1176–1185. https://doi.org/10.1039/c8sc03733g

Jun, Y., Ghose, S., Trainor, T., Eng, P., & Martin, S. (2007). Structure of the hydrated (10-14) surface of rhodochrosite ($MnCO_3$). *Environmental Science & Technology, 41*(11), 3918–3925. https://doi.org/10.1021/es062171v

Kaminski, D., Radenovic, N., Deij, M. A., van Enckevort, W. J. P., & Vlieg, E. (2005). pH-dependent liquid order at the solid-solution interface of KH_2PO_4 crystals. *Physical Review B, 72*(24), Article 245404. https://doi.org/10.1103/PhysRevB.72.245404

Kaminski, D., Radenovic, N., Deij, M. A., van Enckevort, W. J. P., & Vlieg, E. (2006). Liquid ordering at the KDP {100}-solution interface. *Crystal Growth & Design, 6*(2), 588–591. https://doi.org/10.1021/cg0502338

Kim, S., & Baik, S. (1994). X-ray study of step morphology of MgO(100) surfaces. *Applied Surface Science, 78*(3), 285–292. https://doi.org/10.1016/0169-4332(94)90016-7

Kim, S., Baik, S., Kim, H., & Kim, C. (1993). X-ray study of step morphology on a cleaved MgO(100) surface. *Surface Science, 294*(1–2), L935–L938.

Kimball, B. E., Foster, A. L., Seal, R. R., Piatak, N. M., Webb, S. M., & Hammarstrom, J. M. (2016). Copper speciation in variably toxic sediments at the Ely Copper Mine, Vermont, United States. *Environmental Science & Technology, 50*(3), 1126–1136. https://doi.org/10.1021/acs.est.5b04081

Kohli, V., Zhang, Z., Park, C., & Fenter, P. (2010). Rb^{+} and Sr^{2+} Adsorption at the TiO_2 (110)-electrolyte interface observed with resonant anomalous x-ray reflectivity. *Langmuir, 26*(2), 950–958. https://doi.org/10.1021/la902419z

La Plante, E. C., Eng, P. J., Lee, S. S., Sturchio, N. C., Nagy, K. L., & Fenter, P. (2018). Evolution of strain in heteroepitaxial cadmium carbonate overgrowths on dolomite. *Crystal Growth & Design, 18*(5), 2871–2882. https://doi.org/10.1021/acs.cgd.7b01716

La Plante, E., Lee, S., Eng, P., Stubbs, J., Fenter, P., Sturchio, N., & Nagy, K. (2019). Dissolution kinetics of epitaxial cadmium carbonate overgrowths on dolomite. *Acs Earth and Space Chemistry, 3*(2), 212–220. https://doi.org/10.1021/acsearthspacechem.8b00115

Lee, S., Nagy, K., & Fenter, P. (2007). Distribution of barium and fulvic acid at the mica-solution interface using in-situ X-ray reflectivity. *Geochimica et Cosmochimica Acta, 71*(23), 5763–5781. https://doi.org/10.1016/j.gca.2007.05.031

Lee, S., Fenter, P., Park, C., & Nagy, K. (2008). Fulvic acid sorption on muscovite mica as a function of pH and time using in situ X-ray reflectivity. *Langmuir, 24*(15), 7817–7829. https://doi.org/10.1021/la703456t

Lee, S., Nagy, K., Park, C., & Fenter, P. (2009). Enhanced uptake and modified distribution of mercury(II) by fulvic acid on the muscovite (001) Surface. *Environmental Science & Technology, 43*(14), 5295–5300. https://doi.org/10.1021/es900214e

Lee, S., Fenter, P., Park, C., Sturchio, N., & Nagy, K. (2010a). Hydrated cation speciation at the muscovite (001)-water interface. *Langmuir, 26*(22), 16647–16651. https://doi.org/10.1021/la1032866

Lee, S., Park, C., Fenter, P., Sturchio, N., & Nagy, K. (2010b). Competitive adsorption of strontium and fulvic acid at the muscovite-solution interface observed with resonant anomalous X-ray reflectivity. *Geochimica et Cosmochimica Acta, 74*(6), 1762–1776. https://doi.org/10.1016/j.gca.2009.12.010

Lee, S., Nagy, K., Park, C., & Fenter, P. (2011). Heavy metal sorption at the muscovite (001)-fulvic acid interface. *Environmental Science & Technology, 45*(22), 9574–9581. https://doi.org/10.1021/es201323a

Lee, S., Fenter, P., Nagy, K., & Sturchio, N. (2012). Monovalent ion adsorption at the muscovite (001)-solution interface: Relationships among ion coverage and speciation, interfacial water structure, and substrate relaxation. *Langmuir, 28*(23), 8637–8650. https://doi.org/10.1021/la300032h

Lee, S., Fenter, P., Nagy, K., & Sturchio, N. (2013a). Changes in adsorption free energy and speciation during competitive adsorption between monovalent cations at the muscovite (001)- water interface. *Geochimica et Cosmochimica Acta, 123*, 416–426. https://doi.org/10.1016/j.gca.2013.07.033

Lee, S., Schmidt, M., Laanait, N., Sturchio, N., & Fenter, P. (2013b). Investigation of structure, adsorption free energy, and overcharging behavior of trivalent yttrium adsorbed at the muscovite (001)-water interface. *Journal of Physical Chemistry C, 117*(45), 23738–23749. https://doi.org/10.1021/jp407693x

Lee, S., Heberling, F., Sturchio, N., Eng, P., & Fenter, P. (2016). Surface charge of the calcite (104) terrace measured by Rb^{+} adsorption in aqueous solutions using resonant anomalous x-ray reflectivity. *Journal of Physical Chemistry C, 120*(28), 15216–15223. https://doi.org/10.1021/acs.jpcc.6b04364

Lee, S., Fenter, P., Nagy, K., & Sturchio, N. (2017). Real-time observation of cation exchange kinetics and dynamics at the muscovite-water interface. *Nature Communications, 8*, Article ARTN 15826. https://doi.org/10.1038/ncomms15826

Lee, S., Schmidt, M., Sturchio, N., Nagy, K., & Fenter, P. (2019). Effect of pH on the formation of gibbsite-layer films at the muscovite (001)-water interface. *Journal of Physical Chemistry C, 123*(11), 6560–6571. https://doi.org/10.1021/acs.jpcc.8b12122

Liu, X. P., Lin, W., Chen, B., Zhang, F. C., Zhao, P. Q., Parsons, A., Rau, C., & Robinson, I. (2018). Coherent diffraction study of calcite crystallization during the hydration of tricalcium silicate. *Materials & Design, 157*, 251–257. https://doi.org/10.1016/j.matdes.2018.07.031

Lutzenkirchen, J., Heberling, F., Supljika, F., Preocanin, T., Kallay, N., Johann, F., Weisser, L., & Eng, P. (2015). Structure-charge relationship - the case of hematite (001). *Faraday Discussions, 180*, 55–79. https://doi.org/10.1039/c4fd00260a

Magdans, U., Gies, H., Torrelles, X., & Rius, J. (2006). Investigation of the {104} surface of calcite under dry and humid atmospheric conditions with grazing incidence X-ray diffraction (GIXRD). *European Journal of Mineralogy, 18*(1), 83–91. https://doi.org/10.1127/0935-1221/2006/0018-0083

Manceau, A., Lanson, B., Schlegel, M. L., Harge, J. C., Musso, M., Eybert-Berard, L., Hazemann, J.-L., Chateiger, D., & Lamble, G. M. (2000). Quantitative Zn speciation in smelter-contaminated soils by EXAFS spectroscopy. *American Journal of Science, 300*(4), 289–343. https://doi.org/10.2475/ajs.300.4.289

McBriarty, M. E., von Rudorff, G. F., Stubbs, J. E., Eng, P. J., Blumberger, J., & Rosso, K. M. (2017). Dynamic stabilization of metal oxide-water Interfaces. *Journal of the American Chemical Society, 139*(7), 2581–2584. https://doi.org/10.1021/jacs.6b13096

McBriarty, M. E., Stubbs, J. E., Eng, P. J., & Rosso, K. M. (2018). Potential-specific structure at the hematite-electrolyte interface. *Advanced Functional Materials, 28*(8), 1705618. https://doi.org/10.1002/adfm.201705618

McBriarty, M., Stubbs, J., Eng, P., & Rosso, K. (2019). Reductive dissolution mechanisms at the hematite-electrolyte interface probed by in situ x-ray scattering. *Journal of Physical Chemistry C, 123*(13), 8077–8085. https://doi.org/10.1021/acs.jpcc.8b07413

Morin, G., Ostergren, J. D., Juillot, F., Ildefonse, P., Calas, G., & Brown, G. E. (1999). XAFS determination of the chemical form of lead in smelter-contaminated soils and mine tailings: Importance of adsorption processes. *American Mineralogist, 84*(3), 420–434. https://doi.org/10.2138/am-1999-0327

Noerpel, M., Lee, S., & Lenhart, J. (2016). X-ray analyses of lead adsorption on the (001), (110), and (012) hematite surfaces. *Environmental Science & Technology, 50*(22), 12283–12291. https://doi.org/10.1021/acs.est.6b03913

Pareek, A., Torrelles, X., Angermund, K., Rius, J., Magdans, U., & Gies, H. (2009). Competitive adsorption of glycine and water on the fluorapatite (100) surface. *Langmuir, 25*(3), 1453–1458. https://doi.org/10.1021/la802706y

Park, C., Fenter, P., Zhang, Z., Cheng, L., & Sturchio, N. (2004). Structure of the fluorapatite (100)-water interface by high-resolution X-ray reflectivity. *American Mineralogist, 89*(11–12), 1647–1654. https://doi.org/10.2138/am-2004-11-1209

Park, C., Fenter, P. A., Sturchio, N. C., & Regalbuto, J. R. (2005). Probing outer-sphere adsorption of aqueous metal complexes at the oxide-water interface with resonant anomalous X-ray reflectivity. *Physical Review Letters, 94*(7), Article 076104. https://doi.org/10.1103/PhysRevLett.94.076104

Petitto, S., Tanwar, K., Ghose, S., Eng, P., & Trainor, T. (2010). Surface structure of magnetite (111) under hydrated conditions by crystal truncation rod diffraction. *Surface Science, 604*(13–14), 1082–1093. https://doi.org/10.1016/j.susc.2010.03.014

Pfeifer, M. A., Williams, G. J., Vartanyants, I. A., Harder, R., & Robinson, I. K. (2006). Three-dimensional mapping of a deformation field inside a nanocrystal. *Nature, 442*(7098), 63–66. https://doi.org/10.1038/nature04867

Pintea, S., de Poel, W., de Jong, A., Vonk, V., van der Asdonk, P., Drnec, J., Balmes, O., Isern, H., Dufrane, T., Felici, R., & Vlieg, E. (2016). Solid-Liquid Interface Structure of Muscovite Mica in CsCl and RbBr Solutions. *Langmuir, 32*(49), 12955–12965. https://doi.org/10.1021/acs.langmuir.6b02121

Pintea, S., de Poel, W., de Jong, A., Felici, R., & Vlieg, E. (2018). Solid-liquid interface structure of muscovite mica in $SrCl_2$ and $BaCl_2$ solutions. *Langmuir, 34*(14), 4241–4248. https://doi.org/10.1021/acs.langmuir.8b00504

Post, J. E. (1999). Manganese oxide minerals: Crystal structures and economic and environmental significance [Article; Proceedings Paper]. *Proceedings of the National Academy of Sciences of the United States of America, 96*(7), 3447–3454. https://doi.org/10.1073/pnas.96.7.3447

Post, J., & Appleman, D. (1988). Chalcophanite, $ZnMn_3O_7.3H_2O$ - New crystal-structure determinations. *American Mineralogist, 73*(11–12), 1401–1404.

Post, J., & Heaney, P. (2014). Time-resolved synchrotron X-ray diffraction study of the dehydration behavior of chalcophanite. *American Mineralogist, 99*(10), 1956–1961. https://doi.org/10.2138/am-2014-4760

Qiu, C. R., Eng, P. J., Hennig, C., & Schmidt, M. (2018a). Formation and aggregation of ZrO_2 nanoparticles on muscovite (001). *Journal of Physical Chemistry C, 122*(7), 3865–3874. https://doi.org/10.1021/acs.jpcc.7b10101

Qiu, C. R., Majs, F., Eng, P. J., Stubbs, J. E., Douglas, T. A., Schmidt, M., & Trainor, T. P. (2018b). In situ structural study of the surface complexation of lead(II) on the chemically mechanically polished hematite (1-102) surface. *Journal of Colloid and Interface Science, 524*, 65–75. https://doi.org/10.1016/j.jcis.2018.04.005

Reedijk, M. F., Arsic, J., Hollander, F. F. A., de Vries, S. A., & Vlieg, E. (2003). Liquid order at the interface of KDP crystals with water: Evidence for icelike layers. *Physical Review Letters, 90*(6), Article 066103. https://doi.org/10.1103/PhysRevLett.90.066103

Robach, O., Renaud, G., & Barbier, A. (1998). Very-high-quality MgO(001) surfaces: roughness, rumpling and relaxation. *Surface Science, 401*(2), 227–235. https://doi.org/10.1016/S0039-6028(97)01082-0

Robinson, I. (1986). Crystal truncation rods and surface roughness. *Physical Review B, 33*(6), 3830–3836. https://doi.org/10.1103/PhysRevB.33.3830

Robinson, I. K., Vartanyants, I. A., Williams, G. J., Pfeifer, M. A., & Pitney, J. A. (2001). Reconstruction of the shapes of gold nanocrystals using coherent x-ray diffraction. *Physical Review Letters, 87*(19), Article 195505. https://doi.org/10.1103/PhysRevLett.87.195505

Schlegel, M., Nagy, K., Fenter, P., & Sturchio, N. (2002). Structures of quartz (100)- and (101)-water interfaces determined by X-ray reflectivity and atomic force microscopy of natural growth surfaces. *Geochimica et Cosmochimica Acta, 66*(17), 3037–3054. https://doi.org/10.1016/S0016-7037(02)00912-2

Schlegel, M., Nagy, K., Fenter, P., Cheng, L., Sturchio, N., & Jacobsen, S. (2006). Cation sorption on the muscovite (001) surface in chloride solutions using high-resolution X-ray reflectivity. *Geochimica et Cosmochimica Acta, 70*(14), 3549–3565. https://doi.org/10.1016/j.gca.2006.04.011

Schmidt, M., Lee, S., Wilson, R., Soderholm, L., & Fenter, P. (2012a). Sorption of tetravalent thorium on muscovite. *Geochimica et Cosmochimica Acta, 88*, 66–76. https://doi.org/10.1016/j.gca.2012.04.001

Schmidt, M., Wilson, R., Lee, S., Soderholm, L., & Fenter, P. (2012b). Adsorption of plutonium oxide nanoparticles. *Langmuir, 28*(5), 2620–2627. https://doi.org/10.1021/la2037247

Schmidt, M., Lee, S., Wilson, R., Knope, K., Bellucci, F., Eng, P., Stubbs, J., Soderholm, L., & Fenter, P. (2013). Surface-mediated formation of Pu(IV) nanoparticles at the muscovite-electrolyte interface. *Environmental Science & Technology, 47*(24), 14178–14184. https://doi.org/10.1021/es4037258

Schmidt, M., Hellebrandt, S., Knope, K., Lee, S., Stubbs, J., Eng, P., Soderholm, L., & Fenter, P. (2015). Effects of the background

electrolyte on Th(IV) sorption to muscovite mica. *Geochimica et Cosmochimica Acta, 165*, 280–293. https://doi.org/10.1016/j.gca.2015.05.039

Shope, C. L., Xie, Y., & Gammons, C. H. (2006). The influence of hydrous Mn-Zn oxides on diel cycling of Zn in an alkaline stream draining abandoned mine lands. *Applied Geochemistry, 21*(3), 476–491. https://doi.org/10.1016/j.apgeochem.2005.11.004

Stack, A. G., Stubbs, J. E., Srinivasan, S. G., Roy, S., Bryantsev, V. S., Eng, P. J., Custelcean, R., Gordon, A. G, & Hexel, C. R. (2018). Mineral-water interface structure of xenotime (YPO4) {100}. *Journal of Physical Chemistry C*, *122*(35), 20232–20243. https://doi.org/10.1021/acs.jpcc.8b04015

Stubbs, J. E., Chaka, A. M., Ilton, E. S., Biwer, C. A., Engelhard, M. H., Bargar, J. R., & Eng, P. J. (2015). UO_2 oxidative corrosion by nonclassical diffusion. *Physical Review Letters, 114*(24), Article 246103. https://doi.org/10.1103/PhysRevLett.114.246103

Stubbs, J. E., Biwer, C. A., Chaka, A. M., Ilton, E. S., Du, Y., Bargar, J. R., & Eng, P. J. (2017). Oxidative corrosion of the UO_2(001) surface by nonclassical diffusion. *Langmuir, 33*(46), 13189–13196. https://doi.org/10.1021/acs.langmuir.7b02800

Stubbs, J., Legg, B., Lee, S., Dera, P., De Yoreo, J., Fenter, P., & Eng, P. (2019). Epitaxial growth of gibbsite sheets on the basal surface of muscovite mica. *Journal of Physical Chemistry C, 123*(45), 27615–27627. https://doi.org/10.1021/acs.jpcc.9b08219

Tanwar, K., Lo, C., Eng, P., Catalano, J., Walko, D., Brown, G., Waychunas, G., Chaka, A., & Trainor, T. (2007a). Surface diffraction study of the hydrated hematite (1-102) surface. *Surface Science, 601*(2), 460–474. https://doi.org/10.1016/j.susc.2006.10.021

Tanwar, K., Catalano, J., Petitto, S., Ghose, S., Eng, P., & Trainor, T. (2007b). Hydrated alpha-$Fe_2O_3\left(1\bar{1}02\right)$ surface structure: Role of surface preparation. *Surface Science, 601*(12), L59–L64. https://doi.org/10.1016/j.susc.2007.04.115

Tanwar, K., Petitto, S., Ghose, S., Eng, P., & Trainor, T. (2008). Structural study of Fe(II) adsorption on hematite(1-102). *Geochimica et Cosmochimica Acta, 72*(14), 3311–3325. https://doi.org/10.1016/j.gca.2008.04.020

Tanwar, K., Petitto, S., Ghose, S., Eng, P., & Trainor, T. (2009). Fe(II) adsorption on hematite (0001). *Geochimica et Cosmochimica Acta, 73*(15), 4346–4365. https://doi.org/10.1016/j.gca.2009.04.024

Teng, H., Fenter, P., Cheng, L., & Sturchio, N. (2001). Resolving orthoclase dissolution processes with atomic force microscopy and X-ray reflectivity. *Geochimica et Cosmochimica Acta, 65*(20), 3459–3474. https://doi.org/10.1016/S0016-7037(01)00665-2

Trainor, T., Eng, P., Brown, G., Robinson, I., & De Santis, M. (2002). Crystal truncation rod diffraction study of the alpha-Al_2O_3(1-10 2) surface. *Surface Science, 496*(3), 238–250. https://doi.org/10.1016/S0039-6028(01)01617-X

Trainor, T., Chaka, A., Eng, P., Newville, M., Waychunas, G., Catalano, J., & Brown, G. (2004). Structure and reactivity of the hydrated hematite (0001) surface. *Surface Science, 573*(2), 204–224. https://doi.org/10.1016/j.susc.2004.09.040

Trainor, T., Templeton, A., & Eng, P. (2006). Structure and reactivity of environmental interfaces: Application of grazing angle X-ray spectroscopy and long-period X-ray standing waves. *Journal of Electron Spectroscopy and Related Phenomena, 150*(2–3), 66–85. https://doi.org/10.1016/j.elspec.2005.04.011

Vanek, A., Ettler, V., Grygar, T., Boruvka, L., Sebek, O., & Drabek, O. (2008). Combined chemical and mineralogical evidence for heavy metal binding in mining- and smelting-affected alluvial soils. *Pedosphere, 18*(4), 464–478. https://doi.org/10.1016/s1002-0160(08)60037-5

Waychunas, G., Trainor, T., Eng, P., Catalano, J., Brown, G., Davis, J., Rogers, J., & Bargar, J. (2005). Surface complexation studied via combined grazing-incidence EXAFS and surface diffraction: arsenate an hematite (0001) and (10-12). *Analytical and Bioanalytical Chemistry, 383*(1), 12–27. https://doi.org/10.1007/s00216-005-3393-z

Williams, G. J., Pfeifer, M. A., Vartanyants, I. A., & Robinson, I. K. (2006). Internal structure in small Au crystals resolved by three-dimensional inversion of coherent x-ray diffraction. *Physical Review B, 73*(9), Article 094112. https://doi.org/10.1103/PhysRevB.73.094112

Xu, T. Y., Stubbs, J. E., Eng, P. J., & Catalano, J. G. (2018). Response of interfacial water to arsenate adsorption on corundum (001) surfaces: Effects of pH and adsorbate surface coverage. *Geochimica et Cosmochimica Acta, 239*, 198–212. https://doi.org/10.1016/j.gca.2018.07.041

Xu, T., Stubbs, J., Eng, P., & Catalano, J. (2019). Comparative response of interfacial water structure to pH variations and arsenate adsorption on corundum (012) and (001) surfaces. *Geochimica et Cosmochimica Acta, 246*, 406–418. https://doi.org/10.1016/j.gca.2018.12.006

Yan, H., Park, C., Ahn, G., Hong, S., Keane, D., Kenney-Benson, C., Chow, P., Xiao, Y., & Shen, G. (2014). Termination and hydration of forsteritic olivine (010) surface. *Geochimica et Cosmochimica Acta, 145*, 268–280. https://doi.org/10.1016/j.gca.2014.09.005

Yuan, K., Bracco, J., Schmidt, M., Soderholm, L., Fenter, P., & Lee, S. (2019a). Effect of anions on the changes in the structure and adsorption mechanism of zirconium species at the muscovite (001)-water interface. *Journal of Physical Chemistry C, 123*(27), 16699–16710. https://doi.org/10.1021/acs.jpcc.9b02894

Yuan, K., Lee, S. S., Cha, W., Ulvestad, A., Kim, H., Abdilla, B., Sturchio, N., & Fenter, P. (2019b). Oxidation induced strain and defects in magnetite crystals. *Nature Communications, 10*, 10, Article 703. https://doi.org/10.1038/s41467-019-08470-0

Zhang, Z., Fenter, P., Cheng, L., Sturchio, N., Bedzyk, M., Predota, M., & 11 others (2004). Ion adsorption at the rutile-water interface: Linking molecular and macroscopic properties. *Langmuir*, *20*(12), 4954–4969. https://doi.org/10.1021/la0353834

Zhang, Z., Fenter, P., Kelly, S., Catalano, J., Bandura, A., Kubicki, J., & 5 others (2006). Structure of hydrated Zn2+ at the rutile TiO2 (110)-aqueous solution interface: Comparison of X-ray standing wave, X-ray absorption spectroscopy, and density functional theory results. *Geochimica et Cosmochimica Acta*, *70*(16), 4039–4056. https://doi.org/10.1016/j.gca.2006.06.325

Zhang, Z., Fenter, P., Sturchio, N., Bedzyk, M., Machesky, M., & Wesolowski, D. (2007). Structure of rutile TiO2 (110) in water and 1 molal Rb^+ at pH 12: Inter-relationship among surface charge, interfacial hydration structure, and substrate structural displacements. *Surface Science, 601*(4), 1129–1143. https://doi.org/10.1016/j.susc.2006.12.007

(Received: 26 February 2021; revised: 27 August 2021; AE: Geoffrey Bowers)